Polarized neutron reflectometry characterization of interfacial magnetism in an FePt/FeRh exchange spring

W. Griggs [1,*] C. Bull [1] C. W. Barton,[1,†] R. A. Griffiths,[1] A. J. Caruana,[2] C. J. Kinane,[2] P. W. Nutter,[1] and T. Thomson [1]

[1]*NEST Research Group, The Department of Computer Science, The University of Manchester, Oxford Road, Manchester M13 9PL, United Kingdom*

[2]*ISIS, Harwell Science and Innovation Campus, Science and Technology Facilities Council, Rutherford Appleton Laboratory, Didcot, Oxon OX11 0QX, United Kingdom*

We report on the depth-sensitive, temperature-dependent exchange coupling in an FePt/FeRh thin-film exchange-spring structure. The depth-dependent in-plane magnetization is measured as a function of applied magnetic field and sample temperature using polarized neutron reflectometry (PNR). The magnetization profiles are interpreted in terms of the competition between anisotropy, exchange coupling, and dipolar coupling as the FeRh undergoes the magnetic phase transition from antiferromagnetic to ferromagnetic ordering. The PNR data are combined with bulk magnetometry and x-ray characterization, allowing us to determine characteristic length scales over which the exchange-spring mechanism is effective at ambient and elevated temperatures.

I. INTRODUCTION

Systems which exist at the intersection between phases with different magnetic ordering are of great interest, both as a fundamental scientific curiosity and for their potential to be functionalized in next-generation technologies. Of these systems, those in which the competition between the phases can be manipulated with a practicably applicable stimulus have the most promise for implementation in spintronic or data storage devices, where switching efficiency is critical. Equiatomic FeRh presents an excellent example of this kind of system, as it undergoes a first-order phase transition from antiferromagnetic (AFM) to ferromagnetic (FM) ordering at temperatures only moderately above ambience, typically in the range (80–100) °C [1–3]. The characteristics of this phase transition are highly sensitive to a multitude of conditions, including applied magnetic fields [3–5], hydrostatic pressures [6–8], dopant species and concentration [9–11], and both epitaxial [12,13] and piezoelectrically induced [14–17] strains. This tunable magnetic switchability at readily achievable temperatures underpins its candidacy as a material for several novel applications, such as in antiferromagnetic memory resistors [18] and in magnetocalorics [19,20].

Advances in thin-film fabrication techniques have facilitated recent work on alloy composition-tuned systems in which the magnetic ordering or exchange coupling can be graded throughout the depth of a thin-film structure [21–23]. Frequently, polarized neutron reflectometry (PNR) is used to resolve the depth-dependent magnetic properties in these structures [21,22].

Here we present PNR data on an $Fe_{55}Pt_{45}(10)/$ $Fe_{50}Rh_{50}(30)/Pt(1)$ thin-film sample, where the numbers in parentheses denote nominal thicknesses in nanometers. This study follows from our previous work, in which we characterized the nucleation and progression of the FM phase in FeRh using PNR, and elucidate a critical dependence of the magnetic depth profile on surface morphology [24]. The hybrid anisotropy FePt/FeRh structure studied here provides a pathway to an implementation of heat-assisted magnetic recording (HAMR) in which operational temperatures are reduced by the exchange-spring mechanism [25]. Here, the coercivity of the $L1_0$-ordered FePt layer, which has perpendicular magnetic anisotropy (PMA), is reduced when the FeRh layer becomes FM at $\sim$100 °C. This temperature is comparatively lower than the $\sim$500 °C required for currently proposed HAMR, which would alleviate many of the problems that have hindered the implementation of this technology [26]. Although previous studies have investigated the bulk magnetic properties of FeRh/FePt film structures [26–28], a depth-resolved experimental study of their magnetic properties is thus far unreported. Understanding the length scales over which the exchange-mediated effects are prominent in this system is critical to optimizing the layer structure, thus allowing the exchange-spring mechanism to be maximally exploited while minimizing material usage, an important consideration where uncommon metals are required.

PNR measurements were taken over a range of temperature and applied magnetic-field conditions. By fitting scattering-length density (SLD) profiles to the collected data, we elucidate the exchange coupling between adjoining FeRh and FePt through its effect to rotate spins away from their respective anisotropy axes. This allows us to define a characteristic length scale over which the exchange-spring effect occurs. Additionally, we establish the presence of interfacial ferromagnetism in the nominally AFM phase of the FeRh

---

*William.griggs@manchester.ac.uk

†Present address: The National Physical Laboratory, Hampton Road, Teddington TW11 0LW, United Kingdom.

layer, and the effect of this on the neighboring FePt spins is determined.

II. EXPERIMENT METHODS

The FePt/FeRh sample was fabricated by dc magnetron sputtering onto a single-crystal MgO (001) substrate, with a base pressure better than 2×10^{-8} Torr . A 2-nm flash layer was deposited from an $Fe_{50}Pt_{50}$ target to promote good adhesion; then, the remainder of the $Fe_{55}Pt_{45}$ layer was cosputtered at 650 °C from Fe and $Fe_{50}Pt_{50}$ targets, using magnetron powers of 46 and 100 W, respectively. The working gas was Ar at 3-mTorr pressure. The Fe/FePt deposition powers were calibrated using inductively coupled plasma atomic emission spectroscopy to achieve ideal stoichiometry for $L1_0$ ordering. The film was subsequently annealed at 750 °C for 2 h, after which the temperature was set to 600 °C and 30 nm of FeRh was deposited from an $Fe_{50}Rh_{50}$ target. Here, the magnetron power was 100 W and the Ar working pressure was 3 mTorr. The sample was then cooled in the vacuum chamber for 4 h before capping with ∼1 nm of Pt to avoid oxidation (100-W power, 3-mTorr pressure). While it is usual to anneal FeRh for several hours after depositing, this step was omitted here to minimize interdiffusion with the FePt layer, which would significantly modify the physical, chemical, and magnetic properties at the interface.

To confirm the crystallinity of the sample, x-ray diffraction (XRD) measurements were conducted using a Rigaku SmartLab system employing a two-bounce Ge(220) monochromator and producing x rays at the CuK_α edge (wavelength $\lambda =$ 1.541 Å). Measurements were performed in ϑ–2ϑ geometry over the range $2\vartheta =$ (12–88)°, with a step size of 0.01°. Background correction was achieved by subtracting an exponential fit to the baseline signal. Integrated (001) and (002) peak intensities for the FeRh and FePt layers were obtained from Voigt profiles fitted to the XRD data to provide order parameters for each layer. Using the same apparatus, x-ray reflectivity (XRR) measurements were also made, allowing the layer structure to be resolved. XRR data were taken over $2\vartheta =$ (0–4.5)° with a step size of 0.01°. The data were fitted to a dynamical simulation using the open-source software GENX [29]. Here, a differential evolution genetic algorithm is used to minimize a reduced χ^2 figure of merit with respect to layer thicknesses, Gaussian roughnesses, and densities.

Temperature- and field-dependent bulk magnetic properties were measured using vibrating sample magnetometry (VSM) (MicroSense model 10). Here, a circularly cut sister sample of 8-mm diameter was measured, which was fabricated at the same time as the sample used for the PNR measurements. The sample was deionized prior to measurement to prevent erroneous signals from electrostatic buildup. The magnetization was measured over the temperature range (25–200) °C with constant in-plane applied fields of 1 and 7 kOe. Correction for diamagnetic background was achieved by measuring a blank MgO substrate over the same temperature range and subtracting from the FePt/FeRh/Pt measurement data. Out-of-plane hysteresis loops were also measured at a series of temperature setpoints.

The effects of applied magnetic field and temperature on the nuclear and magnetic scattering-length density (n/mSLD)

were probed by PNR using the PolRef beamline at ISIS [30]. The mSLD profile is proportional to the product of the in-plane magnetization and the density of the sample as a function of depth. Prior to measurement, the sample was cleaned in acetone and isopropanol using an ultrasonic bath (5 min each), then affixed to a copper block using a conductive paste to promote good thermal coupling. This arrangement was subsequently baked at 200 °C in vacuum for half an hour to avoid outgassing during the measurement. Spin-polarization resolved reflectivities were measured at incident angles $\vartheta =$ 0.4°, 0.8°, and 1.6°, providing good signal-to-noise over a range of scattering wave vectors $Q =$ (0–0.15) Å^{-1}. The sample temperature was controlled using a direct-contact heating stage in a vacuum furnace equipped with a thermocouple positioned 1 mm from the back of the sample. Once a given temperature setpoint was reached and before any measurements were taken, the arrangement was left to thermalize for at least 1 h to avoid thermometry errors. Measurements were conducted with applied magnetic fields of $H =$ 1 kOe (at 25 and 165 °C) and $H =$ 7 kOe (at 165 °C) to decouple the effects of interlayer exchange and the applied magnetic field on the mSLD.

Extraction of parameters from the PNR data was achieved by fitting the data using GENX [29], with uncertainties calculated using the BUMPS modeling package [31]. Layer thicknesses, densities, roughnesses, and in-plane magnetizations were varied within ranges consistent with the VSM and XRR data. To effectively model the mSLD profiles, the FePt and FeRh layers were subdivided into two layers each, with each sublayer having equal densities but different magnetizations. The roughness between two layers with bulk mSLD β_1 and β_2 is modeled by GENX using a Gaussian mixing function, such that across the interface the mSLD as a function of depth z is given by

$$\beta(z) = E_\sigma(z)\beta_1 + [1 - E_\sigma(z)]\beta_2, \tag{1}$$

where $E_\sigma(z)$ is an integrated Gaussian function where the width σ is centered at the interface.

III. EXPERIMENT RESULTS

The XRD data shown in Fig. S1 of the Supplemental Material [32] confirms that the FePt and FeRh layers are well ordered in the $L1_0$ and $B2$ phases, respectively. Voigt fits to the fundamental and superlattice peaks of FePt and FeRh allow order parameters S to be calculated through $S^{FeRh} =$ $0.935 \times \sqrt{I_{001}/I_{002}}$ [33] and $S^{FePt} = 0.493 \times \sqrt{I_{001}/I_{002}}$ [34], where I_{001} and I_{002} are the integrated intensities of the (001) and (002) diffraction peaks of each material (Supplemental Material, Fig. S2 [32]). This analysis provides $S^{FeRh} = 0.817$ and $S^{FePt} = 0.533$, which are consistent with previously reported values for FeRh [12,35] and FePt [36,37] thin films.

The thicknesses, densities, and roughnesses of each layer were determined by XRR measurements, as shown in Fig. S3 of the Supplemental Material. A dynamical simulation was fitted to the measured reflectivity profile using the GENX reflectivity package [29], resulting in the fitting parameters provided in Table S1 of the Supplemental Material [32]. Thicknesses of (32.4 ± 0.7) nm, (12.8 ± 0.8) nm, and (0.58
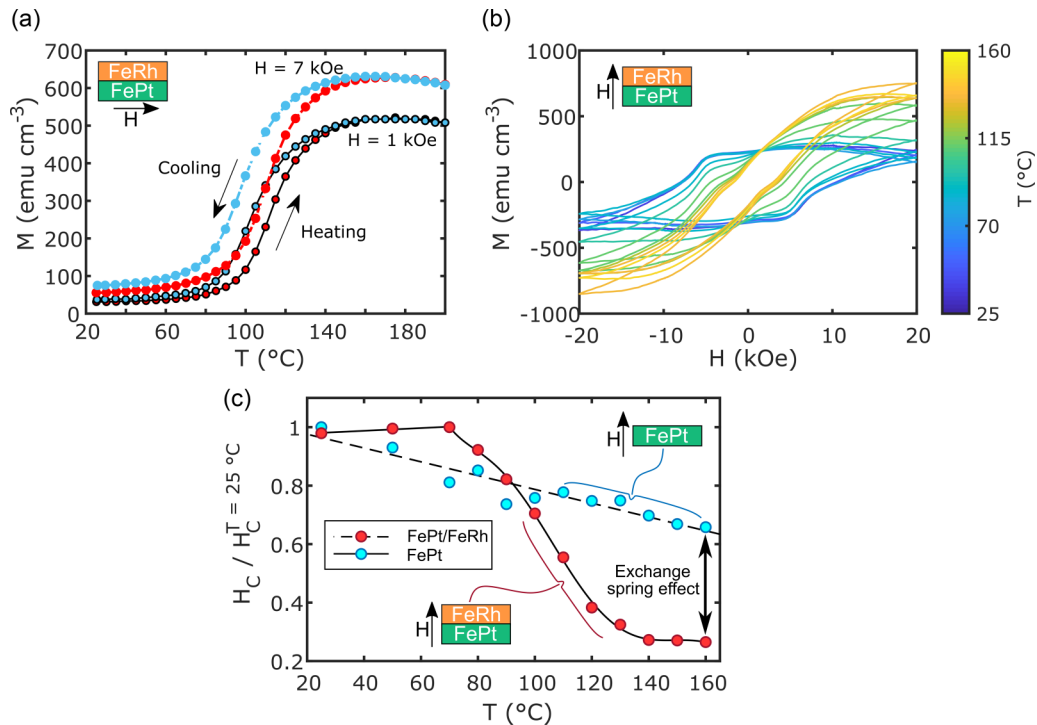
FIG. 1. (a) In-plane magnetization measurements as a function of sample temperature for $H = 1$ kOe and $H = 7$ kOe. The large, hysteretic change in magnetisation on heating is attributed to the MPT in the FeRh layer. (b) Out-of-plane M-H loops measured from the sample at increasing temperature over the range 25–160 °C. (c) The sample coercivity H_c normalized by the value at 25 °C, $H_{T=25\,°C}$, plotted as a function of temperature for the FePt/FeRh bilayer sample (red data) and a single 10-nm FePt film (blue data). Here, the solid and dashed curves are guides to the eye. The data show a large reduction in the FePt/FeRh coercivity, consistent with the presence of an exchange-spring effect.

± 0.06) nm were determined for the FePt, FeRh, and Pt layers respectively.

In-plane thermomagnetic measurements of the sample are shown in Fig. 1(a), where applied magnetic fields of $H = 1$ kOe and $H = 7$ kOe were used. The data demonstrate that the FeRh undergoes a magnetic phase transition (MPT) beginning at $\sim$80 °C, reaching maximum magnetization values of 510 and 648 emu cm^{-3} for the 1- and 7-kOe cases, respectively. Figure 1(b) presents out-of-plane $M - H$ curves as a function of increasing temperature. The data reveal several notable features. First, it is clear that the out-of-plane magnetization response is not saturated at the maximum applied magnetic field of ±20 kOe, since for all temperatures the hysteresis loops are open at these extremal values. Usually, thin-film $L1_0$-ordered FePt with PMA is expected to saturate along the perpendicular direction for applied fields of <15 kOe [38], where the reversal mechanism is one of nucleation followed by domain growth. The fact that the out-of-plane magnetization does not saturate over the full range of applied fields at 25 °C in the present case provides evidence for exchange coupling to the FeRh layer even when it is nominally in the AFM phase.

Further, in all cases the hysteresis is characterized by a complex switching behavior. The small soft component at close to zero applied field across all temperatures is likely a manifestation of a low-anisotropy magnetization at the FePt/FeRh interface. As the temperature is increased, the maximum magnetisation increases as the FeRh transitions to the FM phase. The loop shape is consistent

with the increasing presence of a material with in-plane anisotropy, as it transitions from an essentially square loop at room temperature to a much narrower loop as the MPT progresses.

To verify that the magnetic response of the FePt/FeRh bilayer is consistent with the expected behavior of an exchange spring, Figure 1(c) shows the out-of-plane coercivity H_C given as a fraction of the value at 25 °C ($H_C^{T=25\,°C}$) as the temperature increases. Also shown are similar data from a single 10-nm FePt layer for comparison. For the FePt/FeRh sample there is a clear change in gradient as the FM phase develops, resulting in a reduction of H_C by a factor of $\sim$4 at 160 °C compared to at 25 °C. For comparison, the single FePt layer coercivity is reduced by a factor of $\sim$1.5 over the same temperature range.

To understand the effect of exchange coupling in rotating the FePt and FeRh spins away from their respective anisotropy axes, variable-temperature PNR data were acquired from the sample across a range of temperature and applied magnetic-field conditions encompassing: (i) room temperature with 1-kOe applied field, (ii) 165 °C with 1-kOe applied field, and (iii) 165 °C with 7-kOe applied field. These measurement conditions allow any rotation of the FePt magnetization due to exchange interaction with FM FeRh to be effectively decoupled from the torque exerted on the FePt spins by the external magnetic field. The PNR data are presented in Fig. 2(a). Here, the red and blue symbols denote measured spin-up and -down reflectivities respectively. Dynamical simulations of the reflectivity profiles were fitted to the PNR data using GENX
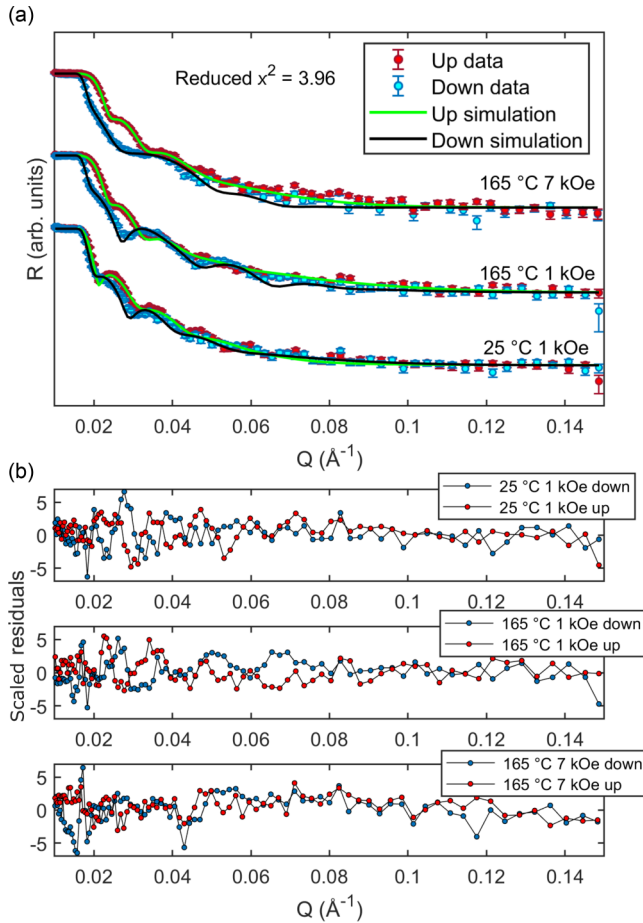
(a)

(b)

FIG. 2. (a) PNR data from the FePt/FeRh bilayer structure at 25 °C with 1-kOe applied field, 165 °C with 1-kOe applied field, and 165 °C with 7-kOe applied field. The red and blue data are the measured spin-up and spin-down neutron reflectivities, respectively. The green and black curves represent fitted spin-up and -down simulations, respectively. Here, all data and simulations have been arbitrarily scaled by multiplicative constants to aid legibility. (b) Residuals of the fits, scaled by the PNR uncertainties. The fits do not show systematic deviations, indicating that the PNR data are appropriately modeled.

[29] (green and black curves in Fig. 2(a) for the spin-up and spin-down reflectivities, respectively).

The procedure for modeling all PNR data began with the assumption that each deposited layer corresponds to a discrete region of uniform magnetic ordering. This proved insufficient to describe the data, producing qualitatively inaccurate fits and reduced $\chi^2 > 10$ in all cases, indicating that the nSLD and mSLD vary independently. Hence, iteratively more complex magnetic and structural configurations were modeled until the reduced χ^2 plateaued, at which point no further magnetic layers were included such to avoid overfitting (Fig. 3). This methodology culminated in the splitting of the FeRh and FePt layers into two discrete sublayers each: a "bulk" layer and an "interfacial" layer, the latter of which is adjacent to the FePt/FeRh interface. The total FeRh and FePt layer thicknesses and densities were fitted using a single parameter across all temperature and applied magnetic-field conditions. Layer roughnesses and magnetizations were allowed to vary
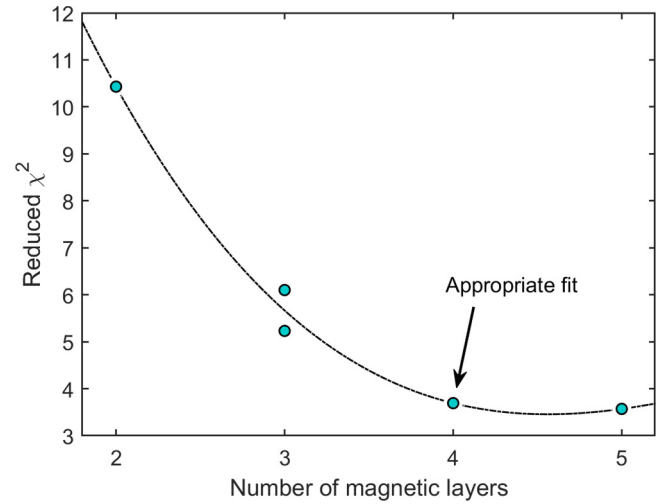

FIG. 3. The reduced χ^2 vs the number of magnetic layers modeled to fit the PNR data (curve is a guide to the eye). The nominal structure comprises FePt, FeRh, and Pt layers. The reduced χ^2 begins to plateau at five layers, which corresponds to a splitting of the FePt and FeRh into two magnetic regions each.

between the 25 °C/1-kOe and 165 °C/1-kOe cases to allow for the possibility of thermally induced interfacial mixing and to model the magnetic phase transition in the FeRh. For the 165 °C/7-kOe case, the roughness of the interfacial FePt sublayer was constrained to its value at 165 °C/1 kOe as this parameter models the interdiffusion between FePt and FeRh, which should not change with the applied field. The parameters used to fit the PNR data are provided in Table S2 of the Supplemental Material.

To demonstrate the validity of the PNR modeling procedure, scaled residuals are shown in Fig. 2(b) for each of the fits, where the differences between each fit and the measured data have been scaled by the measurement uncertainty. The residual plots do not exhibit any notable structure, demonstrating that there are no systematic deviations between the two, and hence validating the model.

From the fits to the PNR data, nSLD and mSLD profiles can be determined, as shown in Figs. 4(a)–4(c). Here, $z = 0$ is the substrate interface, with z increasing towards the film surface. The nSLD profiles (red shaded areas) are the product of the scattering power of the atomic species and their number density, while the mSLD profiles are proportional to the product of the in-plane magnetization and the number density. Here, the vertical lines indicate the positions of the FePt/FeRh and FeRh/Pt interfaces.

To verify that the fitted PNR data are consistent with the bulk magnetometry, the total in-plane moments obtained by integrating over each mSLD profile are plotted alongside the VSM measurements in Fig. 4(d). The PNR and VSM data are consistent over the full range of experimental conditions, providing strong confidence in the fitted parameters.

IV. DISCUSSION

Several previous works have identified a room-temperature FM phase at MgO/FeRh interfaces, which has been attributed
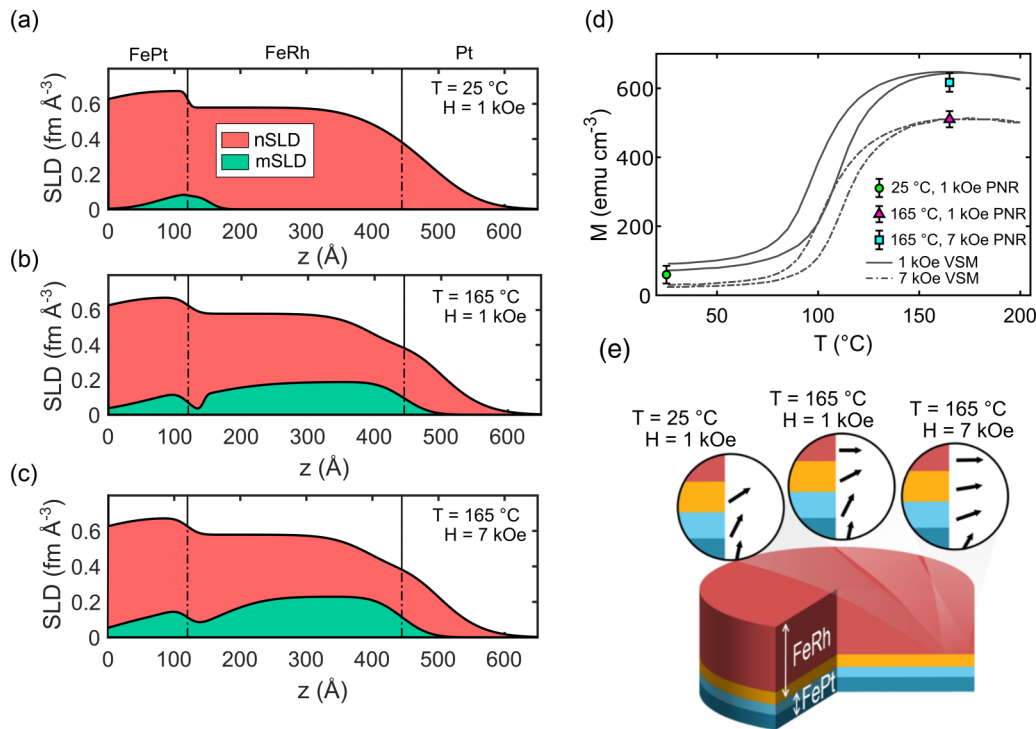
FIG. 4. (a)–(c) Nuclear (nSLD) and magnetic (mSLD) scattering-length density profiles determined from the fits to the PNR data at each temperature and applied magnetic field. The interfaces between FePt, FeRh, and Pt layers are indicated by the vertical lines. (d) The total in-plane moment as a function of temperature as determined by PNR (symbols) and VSM (lines), demonstrating consistency between the two methods. (e) An illustration of the depth-dependent magnetization in the FePt and FeRh layers as a function of temperature and applied magnetic field. There is a substantial interfacial moment in the FeRh layer at 25 °C with 1-kOe applied field, which exerts a torque on the FePt spins via exchange coupling. As the sample is heated, the FeRh layer becomes FM and the exchange-mediated reorientation of the FePt spins is augmented. On increasing the applied field to 7 kOe, the in-plane magnetization increases concomitantly throughout the depth of the bilayer.

to epitaxial strain [39], metallic interdiffusion [24], or the coexistence of α' and γ phases of FeRh during the initial growth due to differences in FeRh–MgO and FeRh–FeRh bond energies [40]. Here, the 25 °C mSLD, shown in Fig. 4(a), reveals that a similar nonzero magnetization is present on both sides of the FeRh/FePt interface. This interfacial FM likely results from Fe migration into the FeRh or Rh migration into the FePt, as the phase transition temperature decreases with decreasing Rh concentration [9]. Hence, we ascribe surplus Fe in the first few nanometers of FeRh as the agent that stabilizes the FM phase.

The form of the 25 °C mSLD reveals that the in-plane magnetization of the FePt layer decays with distance from the interface. The depth-dependent in-plane magnetization in this layer can be explained in terms of spin reorientation from dipolar coupling due to the applied field and exchange coupling with the FM interfacial FeRh, where the strength of the latter interaction decays with distance. Since PNR is sensitive only to the in-plane component of the magnetization, the rotation of spins with increasing distance from the substrate manifests as a reduction of the mSLD. This behavior is illustrated in Fig. 4(e).

As shown in our previous work [24], the FeRh layer is not typically metallically smooth; rather, it features substantial undulations which span several hundred nanometers in the lateral plane. As a result of this morphology, the Pt capping layer reflects this undulation. The FeRh roughness (tabulated

as the roughness of $FeRh_2$ in Table S1 of the Supplemental Material [32]) is approximately 5 nm. However, it is important to note that the crystallographic quality of the FeRh is very good, as shown by the order parameter analysis. This large roughness is also reflected in the magnetization profile, as is expected given that an elemental slice through an area close to the FeRh/Pt interface would show a reduced volume of FeRh with increasing z, which is responsible for the observed smearing of the mSLD profile. However, we do not have reason to suspect that this substantial surface roughness should affect the reliability of the PNR results.

On heating to 165 °C the FeRh layer transitions to FM ordering; hence, the mSLD increases from 0 to 0.2 fm $Å^{-3}$ for the bulk of the layer, as shown in Fig. 4(b). At the same time, the in-plane component of magnetization in the FePt layer increases throughout its thickness, providing a change in the total magnetization from 133 emu cm^{-3} at 25 °C to 168 emu cm^{-3} at 165 °C. This spin reorientation can only result from exchange coupling to the adjoining FeRh layer as the applied field is unchanged from the 25 °C measurement.

Despite the observed stabilization of the FM phase at the interface in the 25 °C case, the data show that at 165 °C there is an ~3-nm region in the FeRh adjacent to the FePt layer in which the magnetization is quenched compared to the bulk of the FeRh film. The reduced mSLD in this region is partially explained by the exchange coupling to the FePt spins, which exert a torque on the FeRh magnetization, thus

rotating it away from the sample plane over a finite distance (see Fig. 4(e)). It is possible that the FePt/FeRh interfacial roughness, found to have a width of 1.4 nm, also affects the saturation magnetization in this region, and thus may contribute to the reduction in the FeRh mSLD close to the FePt. However, the mSLD in this region is less than the bulk values of the FeRh and FePt layers, and so cannot be a result of interfacial mixing alone, as this would result in an mSLD that lies in the range $mSLD_{FeRh} \leqslant mSLD \leqslant mSLD_{FePt}$. To reiterate, the 25 °C mSLD demonstrates that the FM phase is energetically favorable compared to AFM ordering in this region, thus indicating that the reduced in-plane magnetization at high temperature is a consequence of spin reorientation due to exchange coupling between the FM FeRh and FePt. To highlight this point further, a model was constructed in which the mSLD in the interfacial region is forced to lie between the bulk values for the FeRh and FePt layers, as shown in Fig. S4 of the Supplemental Material [32]. The resulting fit to the 165 °C/1-kOe PNR data is poor, producing a reduced χ^2 of 13.42, thus demonstrating that the reduced mSLD in this region is an essential feature of the model.

From the magnetometry data of Fig. 1(a), the total in-plane magnetization at 165 °C is greater by 114 emu cm^{-3} for the 7-kOe case compared to the 1-kOe case. The mSLD profile of Fig. 4(c) reveals that the increase occurs throughout the multilayer structure, demonstrating that the external field plays a significant role in rotating the FePt magnetization towards the in-plane direction. The contribution to the in-plane moment from the FePt layer increases by 64 emu cm^{-3} (normalized to the total FePt/FeRh bilayer thickness), i.e., approximately half of the total increase, meaning that the FeRh layer also contributes significantly to the magnetization enhancement when the external applied field is increased. Single-layer FeRh thin films of this thickness are expected to saturate below 1 kOe [41]; in the present case, however, exchange coupling to the FePt layer means that the FeRh spins close to the interface are partially rotated away from the sample plane. Indeed, as with the 1-kOe case, for a 7-kOe applied field there is a reduction in the mSLD towards the FePt interface resulting from the exchange-mediated rotation of FeRh spins in this region. Here, the effect is reduced compared to the 1-kOe case shown in Fig. 4(b), despite the fact that the data are modeled with identical layer densities, roughnesses, and thicknesses.

The fact that the shape of the mSLD changes independently of structure emphasizes the role of exchange in determining the in-plane magnetization within small distances from the interface. On increasing the field to 7 kOe, the decreased out-of-plane component of the FePt magnetization reduces the effect of exchange to pull FeRh spins away from the sample plane. Hence, the dip in the FeRh mSLD near the FePt interface is less exaggerated in the 7-kOe case compared to the 1-kOe case. This scenario is also illustrated in Fig. 4(e). Thus, the PNR data demonstrate that the exchange coupling between the FePt and FeRh layers plays a significant role to reorientate their respective magnetisations away from their individual anisotropy axes. Importantly, it is evident that the exchange-spring effect is prominent throughout the depth of the FePt layer, since the change in mSLD on heating from 25 to 165 °C is nonzero throughout the layer thickness. The effect is clearly more significant at closer distances to the interface;
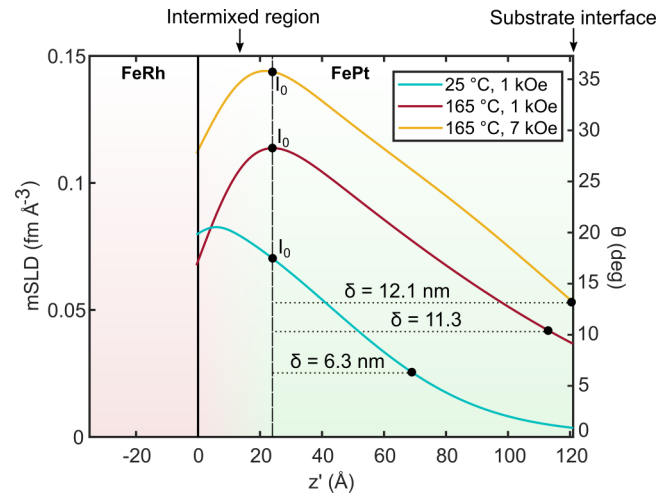

FIG. 5. The decay of the mSLD through the depth of the FePt layer z', where $z' = 0$ is the FeRh/FePt interface and z' increases towards the substrate. The decay lengths δ are characterized by the distance over which the mSLD reduces to $1/e$ of the value at $z' = 2.4$ nm (chosen to avoid effects of interfacial mixing). The mSLD values at $z' = 2.4$ nm are labeled I_0. The right axis allows the same data to be interpreted in terms of the spin angle, where a small angle approximation has been made [Eq. (2)].

hence, the in-plane component of the FePt magnetization decays towards the substrate.

To characterize the length scale of this decay, the distance δ over which the magnitude of the mSLD is reduced by a factor of $1/e$ was calculated, and is shown in Fig. 5. Here, the first 2.4 nm from the FeRh layer were not considered so as to avoid contributions to the mSLD profiles due to interdiffusion at the interface. It should be noted that to emphasize the mSLD decay, here the coordinate z' has been used, which increases towards the substrate with $z' = 0$ being the FePt/FeRh interface. This analysis reveals that the characteristic length scale for the exchange-mediated magnetisation rotation is $\delta = 6.3$ nm for the 25 °C, 1-kOe case, $\delta = 11.3$ nm for the 165 °C, 1-kOe case, and $\delta = 12.1$ nm for the 165 °C, 7-kOe case. These results are summarized in Table I.

The significant difference between the values of δ at 25 and 165 °C can be attributed to temperature dependences of the anisotropy and the exchange constant in the FePt layer. Thus, at the operational temperature of an FePt/FeRh-based HAMR device, i.e., >100 °C, the exchange-spring mechanism

TABLE I. The maximum angle of the FePt spins to the sample normal and the characteristic decay length δ of the spin reorientation due to exchange and magnetostatic couplings. Spin orientation uncertainties were estimated based on the error due to the small angle approximation. Uncertainties on δ are approximated as half the width of the intermixed region.

Conditions	Maximum spin reorientation (°)	δ (nm)
25 °C/1 kOe	20.4 ± 0.4	6.3 ± 1.2
165 °C/1 kOe	29.6 ± 1.3	11.1 ± 1.2
165 °C/7 kOe	38.8 ± 2.9	12.1 ± 1.2

is expected to be effective for FePt thicknesses up to ∼12 nm. This is an essential consideration in the development of devices with optimum performance while minimizing the FePt layer thickness and hence cost.

From the magnetometry of Fig. 1(b), assuming that the FePt is close to saturation at 20 kOe, and using the approximation that the FeRh layer does not contribute to the room-temperature out-of-plane magnetization, the saturation magnetization of the FePt can be calculated to be 820 emu cm^{-3}. Using the PNR-fitted density of 3.54×10^{-2} f.u. Å^{-3}, this magnetization corresponds to 2.50 μB f.u.$^{-1}$, or an mSLD of 0.23 fm Å^{-3}. Thus, it is possible to convert the mSLD profiles to the average spin orientation $\sin\theta$ in the FePt layer, where θ defines the angle between the spin axis and the sample normal, as shown by the right axis of Fig. 5. The conversion is given by

$$\sin\theta = \frac{\text{mSLD}}{0.23 \text{ fm Å}^{-3}}, \qquad (2)$$

where the dependence of the FePt saturation magnetisation on temperature has been ignored; this approximation is justified by the fact that the temperatures probed in this experiment were far from the FePt Curie temperature, ∼500 °C. Indeed, over the range (25–165) °C, it is expected that the FePt saturation magnetization should decrease by no more than 15% [42].

Following this analysis, the FePt spins are found to be at maximum angles to the sample normal of 20.4 °, 29.6 °, and 38.8 ° for the 25 °C/1-kOe, 165 °C/1-kOe, and 165 °C/7-kOe cases, respectively. These values are summarized in Table I.

It is important to acknowledge that the model as presented is subject to a notable limitation in that the manner in which the mSLD decays with distance from the interface varies according to a fitted roughness between two FePt sublayers of equal density but different magnetization. This approach, while effective in avoiding overfitting the PNR data (see Fig. 3), essentially limits the form of the decay to that of an error function. Despite this simplification, the model is effective in describing the broad features of the propagation of exchange coupling in the FePt layer, and provides the magnitude of the spin reorientation at the interface and the length scale of its decay with distance.

V. CONCLUSIONS

In summary, we report the importance of understanding the temperature and applied field-dependent evolution of interlayer coupling in exchange-spring systems with both in-plane anisotropy and PMA. We achieve this by extracting the depth-dependent mSLD profiles from PNR measurements for an FePt/FeRh exchange-spring system and investigate their evolution with temperature and applied magnetic field. Thus, a sensitive manipulation of the orientation of FePt spins has been demonstrated, where the magnitude of the applied magnetic field and the progression of the MPT in FeRh have been identified as playing key roles in the length scale over which this effect is prominent. It has been shown that within the limitations of the model, the characteristic length for the exchange coupling δ increases due to the AFM to FM phase transition. At typical operational temperatures for this system, the exchange-mediated spin reorientation extends across at least the first 12 nm of FePt adjacent to an FeRh layer, representing an estimate of the thickness of an FePt layer in which the write field may be reduced by the exchange-spring effect.

[1] M. Fallot, Les alliages du fer avec les métaux de la famille du platine, Ann. Phys. **10**, 291 (1938).

[2] M. Fallot, Propriétés magnétiques des alliages du fer avec le rhodium, C. R. Hebd Seances Acad. Sci. **205**, 558 (1937).

[3] J. B. McKinnon, D. Melville, and E. W. Lee, The antiferromagnetic-ferromagnetic transition in iron-rhodium alloys, J. Phys. C: Solid State Phys. **3**, S46 (1970).

[4] J. S. Kouvel and C. C. Hartelius, Anomalous magnetic moments and transformations in the ordered alloy FeRh, J. Appl. Phys. **33**, 1343 (1962).

[5] S. Maat, J. Thiele, and E. E. Fullerton, Temperature and field hysteresis of the antiferromagnetic-toferromagnetic phase transition in epitaxial FeRh film, Phys. Rev. B **72**, 214432 (2005).

[6] L. I. Vinokurova, A. V. Vlasov, and N. I. Kulikov, Pressure-induced antiferromagnetism in ferromagnetic Fe$_{51.5}$Rh$_{48.5}$ alloy, J. Magn. Magn. Mater. **25**, 201 (1981).

[7] A. J. Heeger, Pressure dependence of the FeRh first-order phase transition, J. Appl. Phys. **40**, 4751 (1970).

[8] L. I. Vinokurova, A. V. Vlasov, and M. Pardavi- Horváth, Pressure effects on magnetic phase transitions in FeRh and FeRhIr alloys, Phys. Status Solidi **78**, 353 (1976).

[9] E. M. Hofer and P. Cucka, Magnetic properties of Rh-rich FeRh alloy, J. Phys. Chem. Solids **27**, 1552 (1966).

[10] P. H. L. Walter, Exchange inversion in ternary modifications of iron rhodium, J. Appl. Phys **35**, 938 (1964).

[11] R. Barua, F. Jiménez-Villacorta, and L. H. Lewis, Predicting magnetostructural trends in FeRh-based ternary systems, Appl. Phys. Lett. **10**, 102407 (2013).

[12] C. W. Barton, T. A. Ostler, D. Huskisson, C. J. Kinane, S. J. Haigh, G. Hrkac, and T. Thomson, Substrate induced strain field in FeRh epilayers grown on single crystal MgO (001) substrates, Sci. Rep. **7**, 44397 (2017).

[13] X. Zhoua, F. Matthes, D. E. Bürglerb, and C. M. Schneider, Magnetic surface domain imaging of uncapped epitaxial FeRh(001) thin films across the temperature-induced metamagnetic transition, AIP Adv. **6**, 015211 (2016).

[14] Y. Xie, Q. Zhana, T. Shang, H. Yang, Y. Liu, B. Wang, and R.-W. Lia, Electric field control of magnetic properties in FeRh/PMN-PT heterostructures, AIP Adv. **8**, 055816 (2018).

[15] I. Fina, A. Quintana, X. Martí, F. Sánchez, M. Foerster, L. Aballe, J. Sort, and J. Fontcuberta, Reversible and magnetically unassisted voltage-driven switching of magnetization in FeRh/PMN-PT, Appl. Phys. Lett. **113**, 152901 (2018).

[16] Z. Q. Liu, L. Li, Z. Gai, J. D. Clarkson, S. L. Hsu, A. T. Wong, L. S. Fan, M.-W. Lin, C. M. Rouleau, T. Z. Ward *et al.*, Full Electroresistance Modulation in a Mixed-Phase Metallic Alloy, Phys. Rev. Lett. **116**, 097203 (2016).

[17] J. D. Clarkson, I. Fina, Z. Q. Liu, Y. Lee, J. Kim, C. Frontera, K. Cordero, S. Wisotzki, F. Sanchez, J. Sort *et al.*, Hidden magnetic states emergent under electric field, in a room temperature composite magnetoelectric multiferroic, Sci. Rep. **7**, 15460 (2017).

[18] X. Marti, I. Fina, C. Frontera, J. Liu, P. Wadley, Q. He, R. J. Paull, J. D. Clarkson, J. Kudrnovský, I. Turek *et al.*, Room-temperature antiferromagnetic memory resistor, Nat. Mater. **13**, 367 (2014).

[19] S. A. Nikitin, G. Myalikgulyev, A. M. Tishin, M. P. Annaorazov, K. A. Asatryan, and A. L. Tyurin, The magnetocaloric effect in $Fe_{49}Rh_{51}$ compound, Phys. Lett. A **148**, 363 (1990).

[20] M. P. Annaorazov, S. A. Nikitin, A. L. Tyurin, K. A. Asatryan, and A. Kh. Dovletov, Anomalously high entropy change in FeRh alloy, J. Appl. Phys **79**, 1689 (1996).

[21] B. J. Kirby, H. F. Belliveau, D. D. Belyea, P. A. Kienzle, A. J. Grutter, P. Riego, A. Berger, and C. W. Miller, Spatial Evolution of the Ferromagnetic Phase Transition in an Exchange Graded Film, Phys. Rev. Lett. **116**, 047203 (2016).

[22] L. Fallarino, B. J. Kirby, M. Pancaldi, P. Riego, A. L. Balk, C. W. Miller, P. Vavassori, and A. Berger, Magnetic properties of epitaxial CoCr films with depth-dependent exchange-coupling profiles, Phys. Rev. B **95**, 134445 (2017).

[23] L. Fallarino, M. Quintana, E. L. Rojo, and A. Berger, Suppression of Coercivity in Nanoscale Graded Magnetic Materials, Phys. Rev. Appl. **16**, 034038 (2021).

[24] C. Bull, C. W. Barton, W. Griggs, A. Caruana, C. J. Kinane, P. W. Nutter, and T. Thomson, PNR study of the phase transition in FeRh thin films, APL Mater. **7**, 101117 (2019).

[25] J.-U. Thiele, S. Maat, J. L. Robertson, and E. E. Fullerton, Magnetic and structural properties of FePt-FeRh exchange spring films for thermally assisted magnetic recording media, IEEE Trans. Magn. **40**, 2537 (2004).

[26] J. Thiele, S. Maat, and E. E. Fullerton, FeRh/FePt exchange spring films for thermally assisted magnetic recording media, Appl. Phys. Lett. **82**, 2859 (2003).

[27] P. W. Huang and R. H. Victora, Approaching the grain-size limit for jitter using FeRh/FePt in heat-assisted magnetic recording, IEEE Trans. Magn. **50**, 1 (2014).

[28] T. J. Zhoua, K. Cher, J. F. Hu, Z. M. Yuan, and B. Liu, The concept and fabrication of exchange switchable trilayer of FePt/FeRh/FeCo with reduced switching field, J. Appl. Phys. **111**, 07C116 (2012).

[29] M. Björck and G. Andersson, GENX: An extensible X-ray reflectivity refinement program utilizing differential evolution, J. Appl. Crystallogr. **40**, 1174 (2007).

[30] "POLREF," ISIS Neutron and Muon Source (Online). Available: https://www.isis.stfc.ac.uk/Pages/polref.aspx. (Accessed 2 November 2021).

[31] P. A. Kienzle, J. Krycka, N. Patel, and I. Sahin, BUMPS (Version 0.8.0) (Computer Software) (2011).

[32] See Supplemental Material at http://link.aps.org/supplemental/10.1103/PhysRevMaterials.6.024403 for structural characterization of sample and details of PNR fitting procedure.

[33] S. D. Granz and M. H. Kryder, Granular $L1_0$ FePt (001) thin films for heat assisted magnetic recording, J. Magn. Magn. Mater. **324**, 287 (2012).

[34] C. L. Graët, M. A. de Vries, M. McLaren, R. M. D. Brydson, M. Loving, D. Heiman, L. H. Lewis, and C. H. Marrows, Sputter growth and characterization of metamagnetic B2-ordered FeRh epilayers, J. Visualized Exp. **80**, e50603 (2013).

[35] L. Benito, L. Clark, T. P. Almeida, T. A. Moore, D. McGrouther, S. McVitie, and C. H. Marrows, Sputter-engineering a first-order magnetic phase transition in sub-15-nm-thick single-crystal FeRh films, Phys. Rev. Mater. **4**, 123402 (2020).

[36] R. A. Griffiths, J. L. Warren, C. W. Barton, J. J. Miles, P. W. Nutter, and T. Thomson, Temperature-Dependent Studies of Coupled $Fe_{55}Pt_{45}/Fe_{49}Rh_{51}$ Thin Films, Phys. Rev. Appl. **10**, 054015 (2018).

[37] S. Okamoto, N. Kikuchi, O. Kitakami, T. Miyazaki, Y. Shimada, and K. Fukamichi, Chemical-order-dependent magnetic anisotropy and exchange stiffness constant of FePt (001) epitaxial films, Phys. Rev. B **66**, 024413 (2002).

[38] L. S. Huang, J. F. Hu, B. Y. Zong, S. W. Zeng, Ariando, and J. S. Chen, Magnetic properties of $L1_0 -$ FePt/Fe exchange-coupled composite nanodots, J. Phys. D: Appl. Phys. **47**, 245001 (2014).

[39] C. Gatel, B. Warot-Fonrose, N. Biziere, L. A. Rodríguez, D. Reyes, R. Cours, M. Castiella, and M. J. Casanove, Inhomogeneous spatial distribution of the magnetic transition in an iron-rhodium thin film, Nat. Commun. **8**, 15703 (2017).

[40] R. Fan, C. J. Kinane, T. R. Charlton, R. Dorner, M. Ali, M. A. de Vries, R. M. D. Brydson, C. H. Marrows, B. J. Hickey, D. A. Arena *et al.*, Ferromagnetism at the interfaces of antiferromagnetic FeRh epilayers, Phys. Rev. B **82**, 184418 (2010).

[41] W. Griggs, B. Eggert, M. O. Liedke, M. Butterling, A. Wagner, U. Kentsch, E. Hirschmann, M. Grimes, A. J. Caruana, C. Kinane *et al.*, Depth selective magnetic phase coexistence in FeRh thin films, APL Mater **8**, 121103 (2020).

[42] T. Bublat and D. Goll, Temperature dependence of the magnetic properties of $L1_0$-FePt nanostructures and films, J. Appl. Phys. **108**, 113910 (2010).